LLNL-JRNL-809034

Computational examination of two-phase microchannel heat transfer correlations with conjugate heat spreading

B. E. Burk, T. P. Grumstrup, T. A. Bevis, J. Kotovsky, T. M. Bandhauer

April 23, 2020

International Journal of Heat and Mass Transfer

Disclaimer

COMPUTATIONAL EXAMINATION OF TWO-PHASE MICROCHANNEL HEAT TRANSFER CORRELATIONS WITH CONJUGATE HEAT SPREADING

Bryan E. Burk[1], Torben P. Grumstrup[2], Taylor A. Bevis[3], Jack Kotovsky[4], Todd M. Bandhauer[1]*

[1]Interdisciplinary Thermal Science Laboratory, Colorado State University, Fort Collins, CO 80524, USA

[2]RMRS Missoula Fire Science Laboratory, U.S. Forest Service, Missoula, MT 59808, USA

[3]Philips Oral Healthcare, Bothell, WA 98021, USA

[4]Lawrence Livermore National Laboratory, Livermore, CA 94550, USA

email: tband@colostate.edu
phone: 970-491-7357
fax: 970-491-3827
Address:
Colorado State University
Department of Mechanical Engineering
1374 Campus Delivery
Fort Collins, CO 80523

ABSTRACT

Microchannel flow boiling is an attractive thermal management strategy for ever-growing volumetric heat dissipation demands associated with electronic systems. Due to difficulties related to measurement at the microscales, the majority of researchers have chosen to study relatively simple situations with uniform heat flux. However, many applications involve local hotspots which give rise to highly non-uniform heat flux and temperature gradients due to heat spreading. This necessitates the consideration of conjugate heat transfer for accurate analysis.

The current work is aimed at investigating conjugate heat transfer in a two-phase microchannel array. Experimental data was collected on R134a flow boiling heat transfer for very small hydraulic diameter (<100 μm) silicon microchannels with very high heat fluxes (>1 kW cm^{-2}) applied via platinum strip heaters with a footprint size of 1 cm × 1 mm. The collected experimental data was then combined with detailed computational modeling utilizing finite element modeling with COMSOL Multiphysics and MATLAB to examine the applicability of five published heat transfer correlations for use in determining local heat transfer coefficients. A two-phase correlation from Agostini and Bontemps, developed for markedly different test parameters, provided the best computational agreement with an RMS temperature difference from experiment of 3.3°C and a predicted peak perimeter-averaged heat transfer coefficient of 116 MW m^{-2} K^{-1}. Modeling confirms the presence of highly non-uniform local heat flux and correspondingly non-uniform local heat transfer coefficient. The results of this study make clear the need for better micro-scale two-phase correlations developed to predict local heat transfer coefficients at these small scales and high local heat fluxes.

KEY WORDS: Microchannel heat transfer, Two-phase heat transfer, Conjugate heat transfer, Computational modeling

1. INTRODUCTION

Continuous advances in technology over the last few decades have driven the need for ever more powerful, and ever smaller, thermal management systems. Forced convection in microchannels has provided promising solutions to these increasing thermal demands since initial work began in the early 1980s [1]. Today, applications involving micro-electronics and laser diodes are moving towards requiring heat flux removal of ≥ 1 kW cm^{-2}. Effective design of thermal management systems must take into account that in many applications much of this heat is produced at local hot spots and heat spreading can be significant [2,3]. Furthermore, it has also been shown that heat transfer coefficient can vary based on the relative location of hotspots and microchannels [4]. The assumption of 1D conduction made in many current microchannel studies is no longer valid and conjugate heat transfer must be considered [5,6].

Computational modeling can be employed to analyze the conjugate heat problem but requires accurate local heat transfer coefficient correlations to do so. Unfortunately, very few local heat transfer correlations exist for microchannels and currently none are designed for the extreme heat flux ranges mentioned previously. After a brief review of microchannel forced convection, this paper examines five widely used microchannel heat transfer correlations in combination with finite element analysis (FEA) to evaluate their validity when applied to very small hydraulic diameter channels with very high heat flux hotspots. COMSOL Multiphysics is coupled with MATLAB to compare the correlation predictions to previously obtained experimental results.

2. PREVIOUS INVESTIGATIONS AND SCOPE OF PRESENT STUDY

Heat removal from two-phase boiling has a number of advantages over single-phase thermal management, including: reduced pumping power due to a decrease in mass flow rate [7–10], reduced fluid inventory caused by the presence of a low density gas [11–13], improved temperature uniformity of the heat source [8,10–14], and much higher heat transfer coefficients [15–17]. Although these advantages persist, flow boiling in microchannels does have limitations. In addition to a potential increase in pressure drop and flow instability challenges caused by rapid vapor formation inside the channel, heat transfer and pressure drop trends in microchannel flow boiling are complex and are not well understood. More exhaustive reviews on flow boiling can be found in published literature [11,15,18–23], but a brief review is given here.

Two-phase flow dynamics and heat transfer are different in microchannels than in their conventionally sized counterparts. In general, flow pattern maps and heat transfer correlations created for macrochannels do not predict microchannel data satisfactorily [22]. Moreover, there is no clear consensus on when the micro-scale begins and the macro-scale ends. Kew and Cornwell found that conventional correlations worked well for tubes of 2.89 mm and 3.39 mm diameters, but predictions began to diverge for smaller diameters [24]. Kandlikar and Grande [25] proposed that conventional channels, minichannels, and microchannels have hydraulic diameters of $D_h > 3.0$ mm, 0.2 mm $< D_h < 3.0$ mm, and $D_h < 0.2$ mm respectively. Kuznetsov and Shamirzaev [26] have proposed that the micro regime begins when channel width shrinks below a certain capillary constant given by $\delta_c = [2\sigma(\rho_{liq} - \rho_{gas})^{-1} g^{-1}]^{1/2}$. Mehendale et al. [27] proposed a distinction between micro, meso, compact and macro scales with transitions at hydraulic diameters of 100 µm, 1 mm, and 6 mm. What can be agreed upon is that as hydraulic diameters reduce below a certain threshold level, inertial, viscous and surface tension forces significantly influence flow dynamics [17,28]. Additionally, as hydraulic diameter continues to decrease, bubbles become constrained, influencing bubble growth and flow regime [17,20,22,29,30]. These factors, along with others, have led to much confusion in accurately predicting heat transfer coefficients.

Setting aside the issue of what exactly constitutes the micro regime, there is confusion as to which factors affect heat transfer. Published data characterizing microchannel flow boiling heat transfer are often seemingly contradictory. Using 3.15 mm stainless steel tubes and R113, Lazarek and Black [31] determined that heat transfer coefficient was dependent on heat flux but not on mass flux or vapor quality. Owhaib et al. [32] found the same thing with vertical stainless-steel tubes with diameters of 0.826 mm – 1.7 mm. On the other hand, Kuznetsov and Shamirzaev [26] found that heat transfer coefficient was indeed dependent on vapor quality and was only weakly dependent on heat flux for rectangular stainless steel microchannels (D_h = 0.975 mm) with R134a and R21. Sumith et al. [33] found that heat transfer coefficient was dependent on both vapor quality and mass flux for water in stainless steel tubes (D=1.45 mm). Many other authors have also found varying dependencies on these and other factors such as liquid and vapor fluid properties, and channel geometry.

Relatedly, the two main heat transfer mechanisms in flow boiling are nucleate boiling and convective boiling. Nucleate boiling occurs when bubbles form and grow along a superheated channel wall while convective boiling occurs as heat is conducted through the liquid and causes evaporation and thus growth of detached bubbles located in the fluid core. It is clear that the relative importance of these two mechanisms differs with flow regime, but different authors have constructed different flow regime maps [28,34–36]. Much of the discrepancy in heat transfer results can be attributed to the fact that most microchannel flow boiling experiments are performed using relatively small sample sizes. As a result, many of the conclusions drawn from these studies have proved to be valid over only narrow parameter ranges. In 2004, Thome et al. [37] pointed out that "… what can now be fabricated… has vastly outpaced what can be thermally modelled." More recently, Bertsch et al. [16] stated that no existing models were satisfactory, and Kim and Mudawar [23] posited that there exists a lack of predictive tools. Clearly a greater understanding is needed.

Given the current state of technology, it is very difficult to obtain robust data in microchannel flow boiling experiments. Due to the microscale nature, there necessarily exists limited real estate in which to place sensors such as pressure transducers and thermocouples. Even if complex fabrication processes are designed to ideally place such sensors, Szczukiewicz et al. [38] have pointed out that the time scales of relevant phenomena involved in flow boiling are frequently shorter than the response time for thermocouples. Visualization of the relevant phenomena, another key to a complete physical understanding, is also exceedingly difficult for the high flow velocities, small hydraulic diameters and high aspect ratios encountered in microchannel flow boiling. Computational modeling provides an alternative route to experimentation in providing opportunity to explore the fundamental principles of flow boiling.

Though limited by the accuracy of the assumptions made for a computational model, results can still be used to gain valuable insight and to guide further experimental design. In turn, the latest experimental results can be used to refine model assumptions. Employed in parallel, modeling and experimentation have the potential to be a potent tool in furthering our fundamental understanding of flow boiling. The majority of computational studies have utilized CFD modeling and employed either level-set (LS) or volume of fluid (VOF) techniques. Most examine microchannels with single nucleation sites to learn about bubble evolution, flow dynamics and heat transfer [39–44]. While these studies frequently obtain reasonable agreement with experimental findings, they are limited to modeling very simple situations. Modeling becomes much more complex when multiple bubble cycles and multiple nucleation sites are considered. Magnini et al. [45] examined the formation of multiple bubbles at a single nucleation site in a square microchannel and found that bubble size and liquid film thickness were affected by sequential bubbles. They also found that time averaged heat transfer coefficients were ~60% greater for the trailing bubble cycle than for the leading bubble cycle. Zhang et al. [46] used a combined level-set and volume of fluid (CLSVOF) method to examine multiple bubbles from a single nucleation site and found that though departure frequencies matched experimental data, discrepancies existed in axial length. When they attempted to model two nucleation sites, they found that heat flux needed to be increased ~25% for bubble growth rates to match data from Tibiriçá and Ribatski [47].

Great strides have certainly been made with numerical simulations, but it appears that accurate system level modeling of complex 3D flow boiling situations remains a significant challenge. One further limitation that should be mentioned is that of the extreme computational demands as models become more complex. While research is being done into appropriate model simplifications, many of these issues can only be alleviated with advancements in hardware technology. Until then, accurate correlations are crucial to predict microchannel heat sink performance.

The majority of microchannel flow boiling correlations have been developed assuming 1D conduction and uniform heat flux. Experiments can be designed such that these assumptions are fairly accurate but, as has been mentioned, many applications have highly non-uniform heat fluxes, leading to heat spreading. It has even been demonstrated that conjugate heat transfer must be taken into account for accurate predictions in some cases of uniform external heat flux [5,6]. The assumption of 1D conduction becomes ever more inadequate as devices continue to decrease in size and increase in power dissipation. Local heat transfer correlations taking into account local properties must be found. FEA simulations provide a unique opportunity to aid in this discovery.

FEA can be used to test the validity of heat transfer correlations when applied to situations for which they are not specifically designed. Though this has been attempted previously, scant literature exists on the subject. Pellicone et al. [48] combined COMSOL and MATLAB to apply a single heat transfer coefficient correlation and a separate pressure drop correlation to model general heat spreading and characterize the efficiency of stacked channel arrangements. Their model, however, assumes an average heat flux applied to each individual channel, which does not account for significant non-uniformities in local heat flux. The aim of this study is to use conjugate heat transfer models using entirely local properties to compare the predictions of five published heat transfer coefficient correlations with experimental data obtained by Bevis and Bandhauer [49,50].

3. PRIOR EXPERIMENTAL SETUP

In the present study, a test section with a confined heat source is modeled and compared to previously collected data. A brief description of the experimental design is given here, and a more thorough discussion of the test facility design and experimental procedures can be found in Bevis and Bandhauer [49] and Bevis[50]. A diagram of the test section analyzed in the present study is shown in Figure 1 along with terminology used to refer to different regions. The test section consists of a 500 µm layer of silicon into which 125 parallel channels with length, width and depth of 5 mm, 45 µm and 200 µm, respectively, have been etched. Fins with a width of 35 µm separate each channel. The total footprint area of the channels is 10 mm in width by 5 mm in length. Short orifice sections of much smaller diameter are placed at the entry to each channel to act as an inlet restriction to aid in flow stability [51–54]. Inlet and outlet ports connect the test section to the test facility, and inlet and outlet manifolds etched into the chip guide fluid through the channels. A 500 µm layer of borosilicate glass is anodically bonded to the etched surface of the silicon, creating a thermally insulating fluidic seal. A platinum strip 10 mm × 1mm × 100 µm thick is then deposited onto the back side of the chip perpendicular to, and along the midline of, the channels to provide joule heating evenly to each channel.

During testing, inlet fluid temperature, pressure and mass flow rate are fixed. Power is supplied to the heater and base temperature is measured via an infrared pyrometer with a 0.9 mm spot size. Heat flux is increased until the heater temperature reaches a set value, at which point a temperature sweep along the channel area length and width is taken. Heat flux is then increased again until the next desired temperature is reached. This process is continued until a final heater temperature of 60^{o}C is attained. Outlet fluid temperature and pressure are monitored and recorded during testing as well. Due to difficulty in holding inlet temperature and pressure conditions constant across all nominal peak temperatures, the inlet temperature and pressure varied between 11.5^{o}C to 14.5^{o}C and 621.3 kPa to 633.4 kPa, respectively. The specific values are shown in Table 1. Values had reached steady state and drift was minimal during testing at any given temperature. It should be noted here for the pyrometer position is controlled with a high precision, two-axis stage and is centered over the heater at the maximum temperature during a single-phase, low heat flux test prior to the collection of any data. As the heater width of 1 mm is larger than the pyromter spot size of 0.9 mm, a position uncertainty of ±0.1 mm is attributed to measurement locations. It should also be noted that previous calibrations showed the temperature uncertainty of the pyrometer to be ±0.67°C [50].

4. COMPUTATIONAL APPROACH

COMSOL Multiphysics™ [55] (COMSOL) is a finite element analysis tool that solves the coupled heat conduction and convection equations iteratively for each mesh element until convergence at a specified tolerance is reached. In the current study, only the solid channel walls and floor are modeled (Figure 2a). Boundary conditions must be applied to all external surfaces. Flow visualization during the experiments showed no indications of flow maldistribution from channel to channel, and temperature sweeps taken with the infrared pyrometer along the heater (perpendicular to the flow direction) revealed temperature variations of less than +/- 1^{o}C [49,50]. It is assumed that these observations together establish the existence of symmetry among the channels, which allows the modeling of a half channel with adiabatic front and back. Thermal resistance network calculations determined that heat loss from the test section to the environment is less than 0.2% of overall dissipated heat [49,50]. Therefore, the top and bottom surfaces of the model, except where the heater is located, are also assigned adiabatic boundary conditions. The heater location is assigned a net input power specified to match experimental values. Defining the convective boundary condition for the remaining surfaces – the fin wall and channel floor – requires a user specified heat transfer coefficient and a fluid temperature. A summary of boundary conditions used is given in Figure 2b. In the following section, the implementation of the various heat transfer coefficient correlations will be discussed, and the method used to address surprisingly complex issue of fluid temperature will be presented.

5. Heat Transfer Correlations

As stated previously, many microchannel heat transfer correlations apply only to narrow parameter ranges. The current experimental channel has a hydraulic diameter of 73.4 µm, a mass flux of 1478 kg m^{-2} s^{-1}, and an applied heat flux of ~10^{4} kW m^{-2}. No published correlations cover the extreme heat flux or the small hydraulic diameter present in this study which, as has been discussed, is the reason for the current work. Based on a thorough search of available literature and preliminary modeling efforts, the five correlations presented below were chosen because of their closest overall fit to the current data set. The Bertsch et al. [16] and Kim and Mudawar [15] correlations were chosen due to their development corresponding to very large databases. The correlations from Lazarek and Black [31], Agostini and Bontemps [56], and Warrier et al. [35] were chosen for the relatively high heat flux, relatively high mass flow rate, and use of R134a in rectangular channels – similar to the current experimental setup – respectively.

5.1. Bertsch et al.

The correlation presented by Bertsch et al. [16] was developed to fit a large database of 3,899 data points obtained from 14 different studies ranging over 12 different fluids and various channel orientations. Hydraulic diameters for the database ranged from 0.16 mm to 2.92 mm, mass fluxes ranged from 20 kg m^{-2}·s^{-1} to 3000 kg m^{-2} s^{-1} and heat fluxes ranged from 0.4 kW m^{-2} to 115 kW m^{-2}. This correlation, shown below, is based on the Chen formulation and consists of both nucleate and convective boiling terms:

$$h = (1-x)h_{nb} + [1+80(\chi^2-\chi^6)e^{(-0.6\cdot Co)}]h_{cb} \tag{1}$$

$$h_{nb} = 55P_R^{\left(0.12-log_{10}\left(R_P\right)\right)}\left(-log_{10}P_R\right)^{-0.55}M^{-0.5}q''^{0.67} \tag{2}$$

$$h_{cb} = \left(1-x\right)h_{conv,l} + xh_{conv,v} \tag{3}$$

$$h_{conv,i} = \left(3.66 + \frac{0.0668\dfrac{D_h}{L_{ch}}\mathrm{Re}_i\,\mathrm{Pr}_i}{1+0.04\left(\dfrac{D_h}{L_{ch}}\mathrm{Re}_i\,\mathrm{Pr}\right)^{2/3}}\right)\frac{k_l}{D_h} \tag{4}$$

The Cooper [57] correlation, which was developed for pool boiling but has good agreement with pure nucleate boiling in microchannels, was chosen as the nucleate boiling term (Eq. (2)). The Hausen correlation [58] for developing laminar flow was likewise used for the convective boiling term (Eq. (4)). Appropriate suppression and enhancement factors associated with the nucleate and convective boiling terms were fit to the database to arrive at the final heat transfer correlation.

5.2 Kim and Mudawar

Kim and Mudawar [15] developed a correlation to fit a database of 10,805 data points obtained from 37 different sources using a wide range of fluids and both single and multi-channel configurations in several orientations. Hydraulic diameters for the database ranged from 0.349 mm to 6.0 mm and mass fluxes ranged from 33 kg $m^{-2}\cdot s^{-1}$ to 1608 kg m^{-2} s^{-1}. This correlation is shown in Eq.'s (5) through (7) and predicted all data with a MAE of 20.3%. The individual nucleate and convective boiling terms are based on a form suggested by Schrock and Grossman [59].

$$h_{tp} = (h_{nb}{}^2 + h_{cb}{}^2)^{1/2} \tag{5}$$

$$h_{nb} = \left[2345 \left({Bo P_H} \big/ {P_F} \right)^{0.70} P_R^{\,0.38} \left(1 - \chi\right)^{-0.51} \right] h_{db} \tag{6}$$

$$h_{cb} = \left[5.2 \left({Bo P_H} \big/ {P_F} \right)^{0.08} We_{fo}{}^{-0.54} + 3.5 \left(\frac{1}{X_{tt}} \right)^{0.94} \left(\frac{\rho_v}{\rho_l} \right)^{0.25} \right] h_{db} \tag{7}$$

5.3. Lazarek and Black

The Lazarek and Black correlation [31] is based on data from upward and downward vertical flow boiling of R113 in small tubes with an inner diameter of 3.15 mm. Mass fluxes ranged from 125 kg $m^{-2}\cdot s^{-1}$ to 750 kg m^{-2} s^{-1} and heat fluxes ranged from 14 kW m^{-2} to 380 kW m^{-2}. The majority of the authors' data falls within ± 15% (with an r.m.s. error of 9%) of the prediction offered by the developed correlation, shown in Eq. (8).

$$Nu = 30\,\mathrm{Re}_l^{\,0.857}\, Bl^{0.714} \tag{8}$$

5.4. Warrier et al.

The Warrier et al. [35] correlation was developed to fit data obtained from flow boiling of FC-84 in horizontally oriented, parallel, rectangular channels with a hydraulic diameter of 0.75 mm. Mass fluxes ranged from 557 kg m^{-2}·s^{-1} to 1600 kg m^{-2} s^{-1} and heat fluxes ranged from zero up to 59.9 kW m^{-2}. The correlation is shown in Eq. (9).

$$\frac{h_{tp}}{h_{sp,fd}} = 1 + 6.0Bl^{1/16} - 5.3\left(1 - 855Bl\right)\chi^{0.65} \tag{9}$$

The fully developed, single-phase heat transfer coefficient referred to ($h_{sp,fd}$) is a modified Dittus-Boelter equation using 0.00805 as the leading coefficient instead of 0.023. Equation (9) predicted all data within ±28%, though the authors caution that this correlation is valid only over vary narrow parameter ranges.

5.5. Agostini and Bontemps

Agostini and Bontemps [56] experimented with vertical flow of R134a through parallel rectangular channels with a hydraulic diameter of 2.01 mm. Mass fluxes ranged from 90 kg m^{-2}·s^{-1} to 295 kg m^{-2} s^{-1} and heat fluxes ranged from 6 kW m^{-2} to 31.6 kW m^{-2}. The authors found that dryout incipience occurred at a vapor quality of 43%, and thus developed separate correlations for the pre- and post-incipience regions, as shown in Eq.'s (10) and (11). The correlations predicted 83% of the data within an error range of ±20% and 95% of the data within an error range of ±30%.

$$h = 28q''^{2/3}G^{-0.26}\chi^{-0.1} \tag{10}$$

$$h = 28q''^{2/3}G^{-0.64}\chi^{-2.08} \tag{11}$$

5.6. Kim and Mudawar Single-phase

A single-phase liquid region does exist in the present study due to a slight fluid subcooling present at the channel inlet. As heat is absorbed, the fluid temperature in this single-phase region rises until the fluid reaches saturation. Because the two-phase heat transfer coefficient can be roughly an order of magnitude larger than the single-phase coefficient, the correlation used for this single-phase region is of relatively minor importance. Kim and Mudawar [60] fit data from Shah and London [61] to a relation from Copeland [62] for the single-phase correlation used here:

$$Nu = \left\{ \left[1.54 \left(\frac{L_{sp}}{\mathrm{Re}_{sp}\, \mathrm{Pr}_l\, D_h} \right)^{-0.33} \right]^4 + {Nu_3}^4 \right\}^{1/4} \tag{12}$$

$$Nu_3 = 8.235\left(1 - 1.833\beta + 3.767\beta^2 - 5.814\beta^3 + 5.361\beta^4 - 2.0\beta^5\right) \tag{13}$$

6. LOCAL FLUID TEMPERATURE AND PRESSURE

Accurate local heat transfer characterization requires a knowledge of local fluid temperature. In the two-phase region, the local temperature is directly linked to the local pressure, so knowledge of this is needed as well. For the current experimental data, temperature and pressure were measured only before entering and after exiting the test section. No local measurements were made. Thus, it is necessary to determine both the fluid temperature and pressure at the channel inlet, as well as the fluid temperature and pressure profiles along the channel length, by some other means. Correlations were used to address both issues, and their implementation will now be presented.

6.1. Channel Inlet Conditions

It is assumed that the fluid temperature at the channel inlet is equal to that at the upstream sensor due to thermal insulation in the system and minimal temperature difference between the fluid and the environment. Determination of pressure in the channel inlet, however, is not as simple. Significant pressure drop occurs between the upstream sensor and the channel inlet, particularly in the restrictive orifice. The Bosch process utilized in test piece fabrication results in varying etch depth profiles near regions of sudden change in feature width (e.g., from manifold to orifice and from orifice to channel). Characterization of this profile proved impractical, resulting in an inability to use CFD for pressure drop analysis. Indeed, initial CFD attempts showed pressure drop through the orifice to be extremely sensitive to the prescribed depth profile. Instead, a correlational method was used to estimate the channel inlet pressure.

Single-phase pressure drop between the upstream and downstream sensors was measured experimentally (ΔP_{meas}) for three slightly different flow rates (99.3 g min^{-1}, 99.6 g min^{-1}, 100.5 g min^{-1}). This measured drop consists of pressure loss between the upstream sensor and the orifice (ΔP_{up}), pressure loss through the orifice (ΔP_{ori}), and pressure loss between the channel inlet and the downstream sensor (ΔP_{down}), as follows:

$$\Delta P_{meas} = \Delta P_{up} + \Delta P_{ori} + \Delta P_{down} \tag{14}$$

Correlations can be employed to estimate ΔP_{up} and ΔP_{down} since geometries are well defined in those regions. Once these values are obtained, ΔP_{ori} can be obtained directly by rearranging Eq. (14).

$$\Delta P_{ori} = \Delta P_{tot} - \Delta P_{up} - \Delta P_{down} \tag{15}$$

Figure 3 depicts the upstream, downstream and orifice regions. Pressure losses for ΔP_{up} and ΔP_{down} were calculated in the typical fashion with friction factors found using the Churchill [63] and Shah and London [61] equations and minor loss coefficients calculated in EES according to [64]. A detailed description of correlational method employed is given in Bevis et al. [65]. Calculated pressure drops through the orifice for the three single-phase cases were 35.4 ± 4.7 kPa, 36.0 ± 4.4 kPa and 38.8 ± 4.6 kPa. The average value of 36.7 ± 2.6 kPa was used to determine the channel inlet pressure for the two-phase data.

6.2. Channel Pressure Profiles

Pressure drop for two-phase flow in microchannels can be substantial. Local fluid saturation temperature, and thus heat transfer behavior, is dependent on local pressure; and local pressure is dependent on pressure drop, which is dependent on vapor quality and thus indirectly dependent on heat transfer. For this reason, the heat transfer and pressure drop problems must be solved together. The approach taken here is that the heat transfer equations are solved first in COMSOL using an estimated pressure distribution. These results are exported to MATLAB, where a new pressure distribution is calculated. COMSOL then solves the heat transfer equations again. This process repeats in an iterative manner until the local pressure at each location in the channel has met the convergence criterion (<50 Pa). No published pressure drop correlations cover the small hydraulic diameter of 73.4 µm used here, so single- and two-phase correlations presented by Lee and Garimella [66], which showed good agreement with data for hydraulic diameters ranging from 160 µm to 538 µm, are used in the present study. These are shown in Eq.'s (16) through (22).

Lee and Garimella Single-phase Pressure Drop

$$\Delta P_{sp} = \frac{1}{2} G^2 v_l f_{sp} L_{sp} \tag{16}$$

$$f_{sp} = \frac{96}{\mathrm{Re}_l}\left(1 - 1.3553\beta + 1.9467\beta^2 - 1.7012\beta^3 + 0.9564\beta^4 - 0.2537\beta^5\right) \tag{17}$$

Lee and Garimella Two-phase Pressure Drop

$$\Delta P_{tp} = \Delta P_{tp,f} + \Delta P_{tp,a} \tag{18}$$

$$\Delta P_{\mathrm{tp,f}} = \frac{L_{\mathrm{sp}}}{\chi} \int_0^{\chi} 2\phi^2 f G^2 \frac{(1-x)^2}{\rho_{\mathrm{l}} D_{\mathrm{h}}} d\chi \tag{19}$$

$$\phi = \sqrt{1 + \frac{C}{X_{vv}} + \frac{1}{X_{vv}^{2}}} \tag{20}$$

$$C = 2566 \cdot G^{0.5466} D_h^{0.8819} \left(1 - e^{-319 D_h}\right) \tag{21}$$

$$\Delta P_{tp,a} = \frac{G^2}{\rho_l} \left[\frac{\chi^2}{\alpha \left(\rho_l \big/ \rho_v \right)} + \frac{(1-\chi)^2}{1-\alpha} - 1 \right] \tag{22}$$

Figure 4 shows the local pressure as function of centerline distance from the upstream pressure sensor to the channel exit for a sample case. The inlet pressure in this case is 633.4 kPa and the estimated outlet pressure is 530.1 kPa.

7. MESHING

Prior to solving the heat transfer model, a mesh specifying element size and shape was applied to the geometry. The mesh was created by casting a quad element mask on one end of the geometry and sweeping it down the length of the channel. Further divisions were added in the axial direction to create finer elements. The central 1.5 mm of the channel (midsection) consists of finer divisions than the rest of the geometry (inlet/outlet section) to account for greater expected thermal gradients in the region directly above the heater. Rectangular elements on faces where heat transfer occurred were further split with diagonals for compatibility with certain built-in COMSOL functions. The mesh is shown in Figure 5.

A mesh sensitivity study revealed that maximum element size of ¼ the fin width for the quad mask, and a maximum size of 1/20th of the channel length and 1/40th of the channel length for the inlet/outlet sections and midsection, respectively, was sufficient to achieve mesh convergence. This resulted in 11,803 elements. When compared to a mesh with over 90,000 elements, temperature and pressure drop measurements differed by less than 0.5%. This proved true with intermediate mesh sizes as well. A similar study with pressure drop revealed that segment lengths of 50 μm was sufficiently small for accurate pressure determination. Convergence tolerance in COMSOL was set to 0.01 and convergence in pressure distribution was set to a maximum difference for any given segment of 50 Pa (<0.2% of total channel pressure drop).

8. RESULTS AND DISCUSSION

Experimental heat transfer coefficients are typically estimated using temperature differences and an assumed knowledge of the heat flux. Due to the extreme applied heat flux and consequent heat spreading in the present study, the local heat flux is variable and unknown. Figure 6a shows the predicted 3D local heat flux distribution using the Bertsch et al. [16] correlation for the 60°C case. Results for the other models are similar, showing that local heat flux is indeed highly non-uniform. The fact that local heat transfer coefficient is a function of local heat flux, complicates matters even further. As shown in Figure 6, there is a significant amount of heat rejection at the fluid-wall interface concentrated near the channel wall, especially in the area directly above the heater. The transition from single-phase to two-phase flow is also shown by the significant increase in the local heat transfer coefficient near the midpoint of the channel in the direction of flow. From this point onward, the pattern of the local heat transfer coefficient matches the pattern for the local heat flux, each showing high non-uniformity in the vertical and axial directions. Thus, for the current study, heat transfer coefficient cannot be used as a metric for comparison.

To evaluate the applicability of difference heat transfer correlations, model base temperatures are compared to experimental measurements. Figures 7a,b,c show comparisons for the 40°C, 50°C, and 60°C cases, respectively. The presence of symmetry allows for the extrapolation of temperature measurements from the single half-channel model to a theoretical array of parallel channels. The model data has been averaged across a circular area with a radius of 0.45 mm to allow accurate comparison to experimental data obtained from the infrared pyrometer, which had a spot size of 0.9 mm [50]. Locations within 0.45 mm of the channel inlet and exit are averaged as far as possible.

The root mean square (RMS) difference of predicted temperature from experimentally measured temperature is used to compare overall performance in the discussion that follows in lieu of heat transfer coefficient. This value was calculated for all models as follows:

$$\Delta T_{RMS} = \sqrt{\frac{1}{n}\sum_{1}^{n}\left(T_{actual,i} - T_{predicted,i}\right)^{2}} \tag{23}$$

where the index ‘*i*’ denotes individual temperature measurement locations along the channel length. Due to interplay between local pressure, heat transfer coefficient and heat spreading, it is difficult to draw specific conclusions as to what adjustments might be made to increase model accuracy. As such, model agreement will be discussed first, followed by one suggestion on potential correlation improvement. Separate RMS difference values were calculated for the single and two-phase regions as well as across the entire channel length, with the single to two-phase transition location determined from model results. These results are shown in Table 2. If transition location coincided with one the of the temperature comparison locations, the data was included in the two-phase RMS calculations. All model transition locations occurred in a range from 1.65 mm to 2.70 mm downstream of the channel inlet, while experimental transition locations were found to occur in a range from 2.10 mm to 2.50 mm. The only models to fall outside the range of agreement were the Kim and Mudawar and the Lazarek and Black models for the 40°C case, which had model values of 2.70 mm and 2.65 mm, respectively, and the Warrier et al. models for the 50°C and 60°C cases, which had values of 1.65 mm and 1.85 mm, respectively.

As can be seen in Figure 7, the Bertsch et al. and Agostini and Bontemps models slightly overpredict the single-phase region temperature for all cases while the Lazarek and Black and the Kim and Mudawar models yield very accurate predictions. For the two-phase region, the Bertsch et al. model underpredicts the temperature for the 40°C case, but agreement improves as input power increases until both yield fairly good predictions for the 60°C case. The Agostini and Bontemps model shows fairly good two-phase region temperature agreement for all three temperature cases. On the other hand, the Lazarek and Black and the Kim and Mudawar models greatly underestimate temperatures in the two-phase region. The Warrier et al. models severely overpredict temperatures in all regions. These trends are captured in the RMS difference values. The best single-phase agreement was obtained from the Lazarek and Black and the Kim and Mudawar models, with average RMS temperature difference across all temperature cases of 0.9°C and 1.0°C, respectively, followed by the Agostini and Bontemps, Bertsch et al. and Warrier et al. models, with average RMS differences of 3.3°C, 3.8^{o}C and 12.9°C, respectively. The best two-phase agreement was obtained by the Agostini and Bontemps and the Bertsch et al. models, with average RMS differences of 2.2°C and 2.8°C, respectively, followed by the Lazarek and Black, the Kim and Mudawar and the Warrier et al. models, with average RMS differences of 7.3°C, 7.6°C and 14.3°C, respectively. When the channel is considered as a whole, the best overall agreement was obtained from the Agostini and Bontemps and the Bertsch et al. models, with average RMS differences of 2.8°C and 3.3°C, respectively, followed by the Lazarek and Black, the Kim and Mudawar, and the Warrier et al. models with average RMS differences of 5.3°C, 5.6°C and 13.7°C, respectively.

Figure 8 shows the heat transfer coefficienct averaged over the heated perimeter of the channel (along the walls and floor) as a function of axial channel location for the 60^{o}C case. Single-phase values vary by less than 1.1% across all models. Peak two-phase values, however, vary widely, with the Kim and Mudawar, and Lazarek and Black models predicting values that are ~3x greater than those of any other model. Higher two-phase HTCs result in a shift in the heat spreading profile, with proportionally more heat transfer occurring in the two-phase region (Figure 9), causing a downstream shift in the transition location. These shifts are relatively mild due to small Biot numbers that grow even smaller with higher heat fluxes.

The percentage of total heat transfer in the single- and two-phase regions are given in Table 3 for all models. Linear interpolation was used if the transition location lay between two data points. Note that the average percentage of heat transfer in the two-phase region increases from 63.3% ± 1.1% in the 40°C case up to 76.9% ± 2.8% in the 50°C case. The trend is muted in the 60°C case due to the presence of a lower inlet fluid temperature. This results in a subsequently greater amount of sensible heat to raise the fluid temperature to the saturation point and, thus, a significant increase in the amount of single-phase heat transfer. Despite this sensible heat, the average percentage of heat transfer in the two-phase region for the 60°C case is 75.8% ± 1.3%, nearly equal to that in the 50°C case, supporting the trend of increased two-phase heat transfer with higher two-phase HTCs.The total amount of heat dissipated in the single-phase region, which is equal to the sensible heat, can be considered constant for any given input power despite minor changes in transition location across the models. As discussed, higher two-phase heat transfer coefficients lead to transition locations further downstream which result in an increase in single-phase surface area for the same amount of heat dissipation. Given that single-phase heat transfer coefficient is roughly constant, one would expect this to mean lower driving temperature differences between the fluid and the silicon which is what is seen in Figure 7. Since the single-phase model data matches closely to experimental data only when two-phase heat transfer coefficients are clearly too high (Kim and Mudawar, Lazarek and Black) one might also expect that simply increasing the single-phase heat transfer coefficient might improve the single-phase temperature agreement for the models that obtained better two-phase heat transfer coefficient agreement. Figure 10 shows the base temperature results when the single-phase heat transfer coefficient is simply multiplied by a factor 1.2 in the 60°C Agostini and Bontemps model. As can be seen, model agreement increases substantially when single-phase HTC is increased. The single-phase RMS difference value decreases from 5.0°C to 2.7°C and the two-phase value decreases from 2.9°C to 2.5°C. Similar decreases are seen in the 40°C and 50°C models as well (Table 4). This fact is perhaps indicative of jetting at the channel inlet leading to a increase in expected HTC.

One final point worth considering is the dominant mechanism of heat transfer in this study and what insight that might lend to developing better correlations. Figure 11 shows the relatively contributions of both nucleate and convective boiling to the overall heat transfer coefficient as predicted by the Bertsch et al. and Kum and Mudawar correlations. Though the overall magnitudes of heat transfer coefficient differ, both correlations predict the substantial dominance of nucleate boiling. That the predicted magnitudes differ significantly, and that the Bertsch et al. correlations yielded better agreement than the Kim and Mudawar correlation suggests that future work aimed at understanding and predicting nucleate boiling heat transfer in microscale channels with very high heat fluxes should be of utmost importance.

9.CONCLUSIONS

The current study used FEA modeling to explore the validity of employing existing microchannel flow boiling correlations to cutting edge applications requiring higher heat fluxes and smaller hydraulic diameters. Due to extreme applied heat flux, heat spreading is present and local heat flux, as well as local heat transfer coefficient, is highly variable. The best computational agreement was found in models employing two-phase heat transfer correlations from Agostini and Bontemps, and Bertsch et al. This agreement was further shown to be significantly improved by uniformly increasing the single-phase heat transfer coefficient by 20%. The need for considering conjugate heat transfer is clear and the computational model presented in this work is a valuable tool for investigating heat removal at very small scales. Further computational examination of these and other correlations, combined with further experimental investigation of microscale flow boiling and pressure drop, should be carried out to lead to a better understanding of the nature of conjugate heat transfer on the microscale and ultimately lead to better predictive tools to guide heat sink design in this new age.

ACKNOWLEDGEMENTS

The authors gratefully acknowledge the support of Lawrence Livermore National Security, LLC, and the Micro and Nano Technology Center at Lawrence Livermore National Laboratory, for funding this effort and providing the test sections.

FUNDING

Funding to Colorado State University was provided by Lawrence Livermore National Security, LLC. Lawrence Livermore National Laboratory is operated by Lawrence Livermore National Security, LLC, for the U.S. Department of Energy, National Nuclear Security Administration under Contract DE-AC52-07NA27344. Document release: LLNL-JRNL-809034.

NOMENCLATURE

Variable	**Description**	**Units/Formula**
Bo	Bond number	$Bo=\frac{g\left(\rho_l-\rho_v\right)D_h^2}{\sigma}$
Bl	Boiling number	$Bl=\frac{q''}{Gh_{fg}}$
Co	Coburn number	$Co=\frac{1}{D_h}\sqrt{\frac{\sigma}{g\left(\rho_l-\rho_v\right)}}$
D_h	Hydraulic diameter	m
f	Friction factor	-
G	Mass flux	kg m^{-2} s^{-1}
h	Heat transfer coefficient	W m^{-2} K^{-1}
h_{db}	Dittus-Boelter heat transfer coefficient	$h_{db}=\left(\frac{k}{D}\right)0.023Re^{4/5}Pr^{2/5}$
k	Conductivity	W m^{-1} K^{-1}
L	Length	m
M	Molecular Mass of fluid	kg $kmol^{-1}$
P_{crit}	Critical pressure	kPa
P_F	Wetted perimeter	m
P_H	Heated perimeter	m
P_R	Reduced pressure	$P_R=\frac{P}{P_{crit}}$
Pr	Prandtl number	-
q''	Heat flux	W m^{-2}
Re	Reynolds number	$Re=\frac{\rho uD}{\mu}$
u	Velocity	m s^{-2}
v	Specific volume	m^3 kg^{-1}
We	Weber number	$We=\frac{G^2D_h}{\rho\sigma}$
$X_{vv/tt}$	Lockhart and Martinelli parameter	-
Greek and Latin		
α	Void fraction	-
β	Aspect Ratio	width/length
Δ	Difference	-
ϵ	Surface roughness	µm
ρ	Density	kg m^{-3}
χ	Vapor quality	-

Subscripts

a	Accelerational
cb	Convective boiling
conv	Convection
ch	Channel
f	Frictional
fd	Fully developed
fo	Fluid only
l	Liquid
min	Minor
nb	Nucleate boiling
sp	Single-phase
tp	Two-phase
v	Vapor

a	Accelerational
cb	Convective boiling
conv	Convection
ch	Channel
f	Frictional
fd	Fully developed
fo	Fluid only
l	Liquid
min	Minor
nb	Nucleate boiling
sp	Single-phase
tp	Two-phase
v	Vapor

List of Figures

List of Tables

Figures

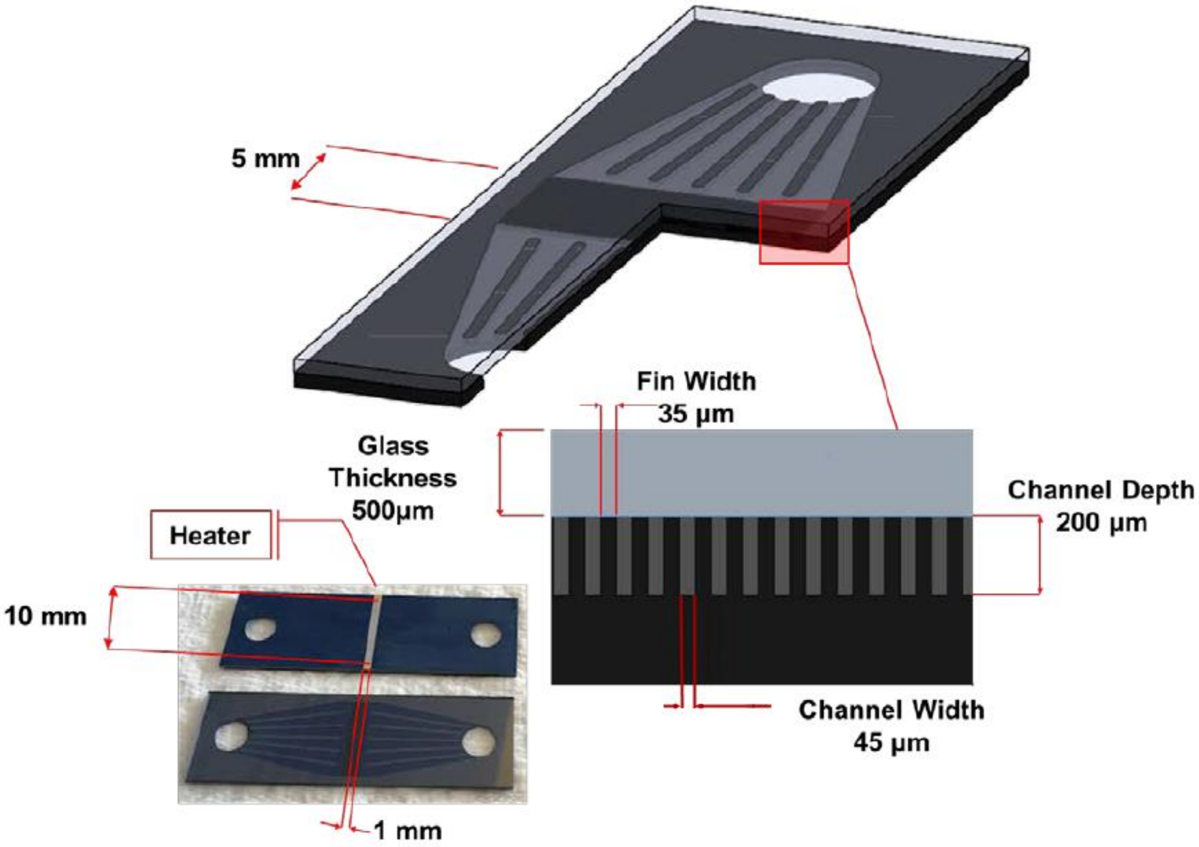

Figure 1. Test section diagram.

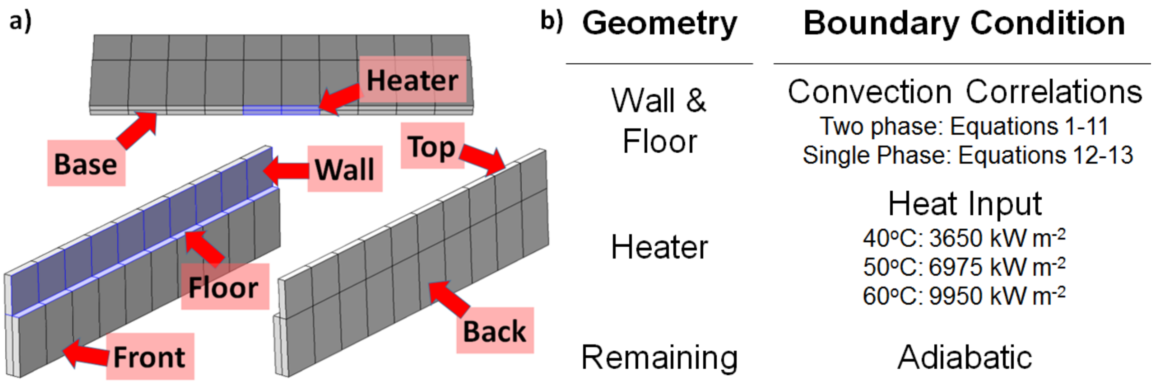

Geometry	Boundary Condition
Wall & Floor	Convection Correlations Two phase: Equations 1-11 Single Phase: Equations 12-13
Heater	Heat Input 40°C: 3650 kW m^{-2} 50°C: 6975 kW m^{-2} 60°C: 9950 kW m^{-2}
Remaining	Adiabatic

Figure 2. (a) Model geometry and (b) and boundary conditions.

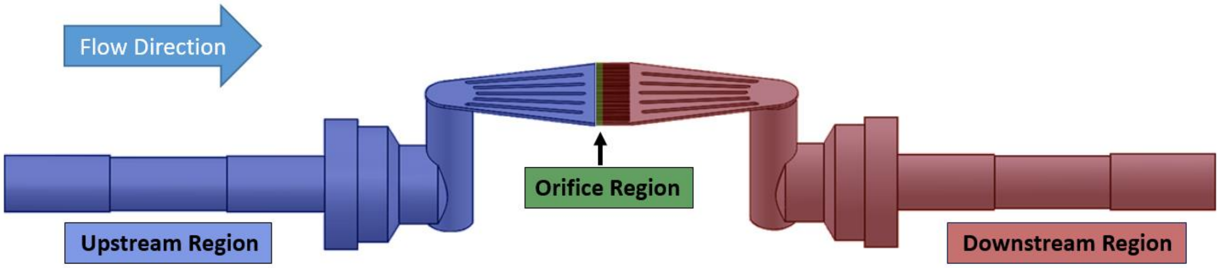

Figure 3. Fluid flow path and regions of calculated pressure losses.

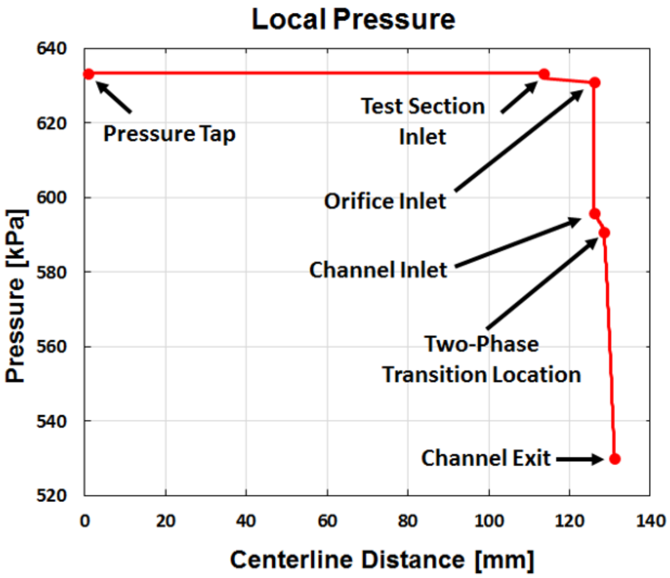

Figure 4. Estimated local pressure between the upstream pressure sensor and the channel exit for the Bertsch et al. 60°C model.

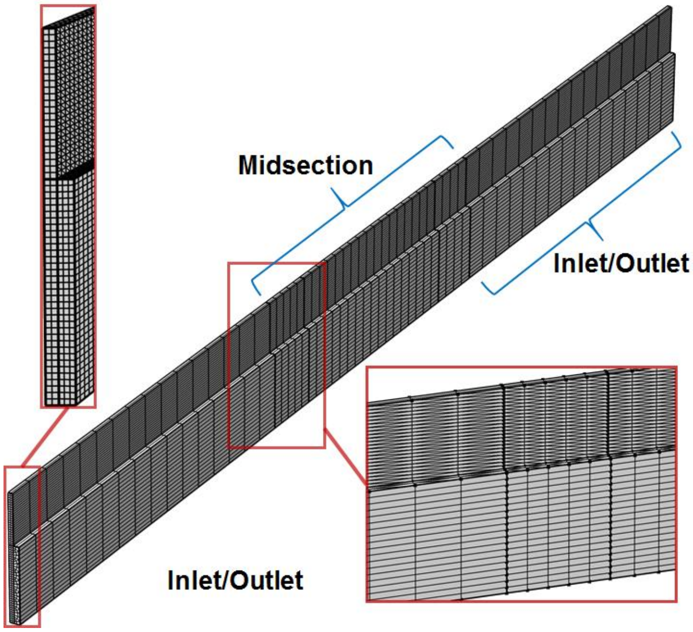

Figure 5. FEA mesh applied to model geometry.

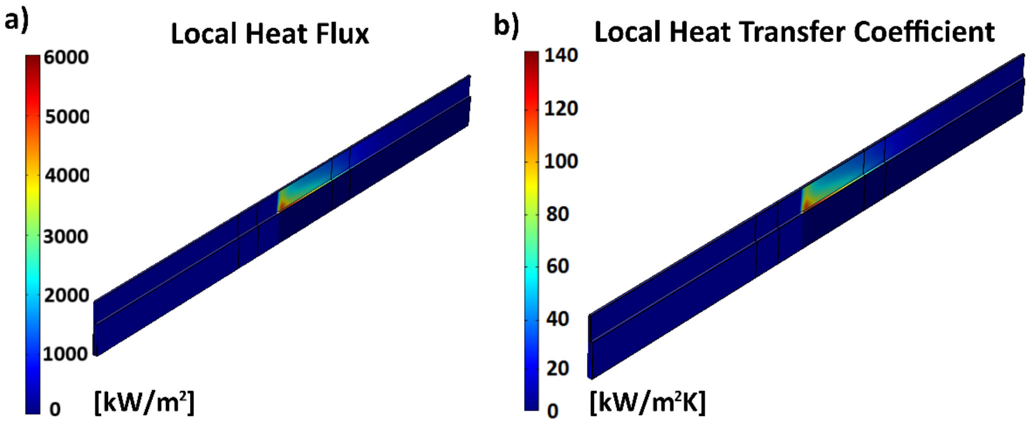

Figure 6. 3D local (a) heat flux and (b) heat transfer coefficient for the Bertsch et al. 60°C model.

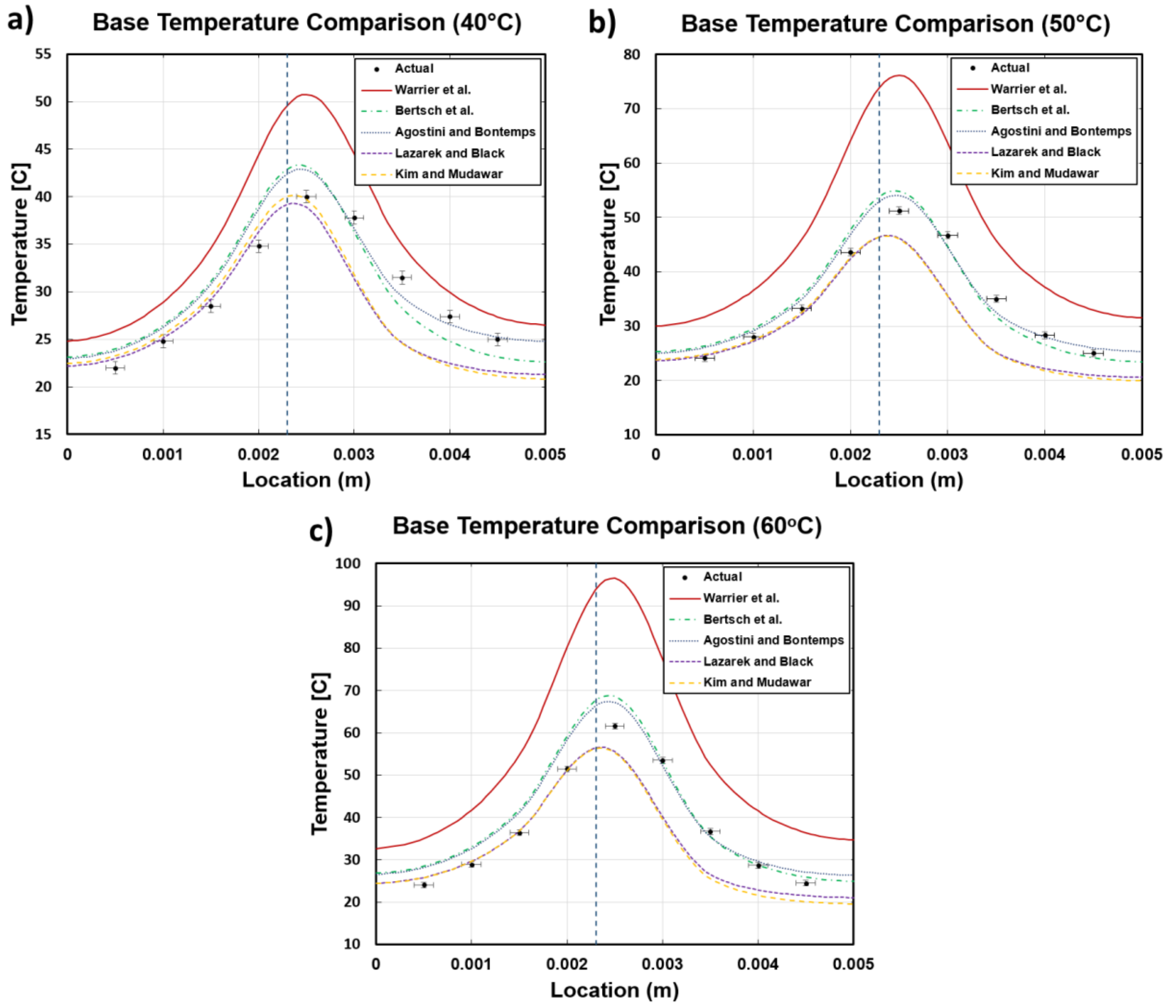

Figure 7. Experimental versus predicted base temperatures for (a) 40°C, (b) 50°C and (c) 60°C cases. Experimental transition location denoted by dotted line.

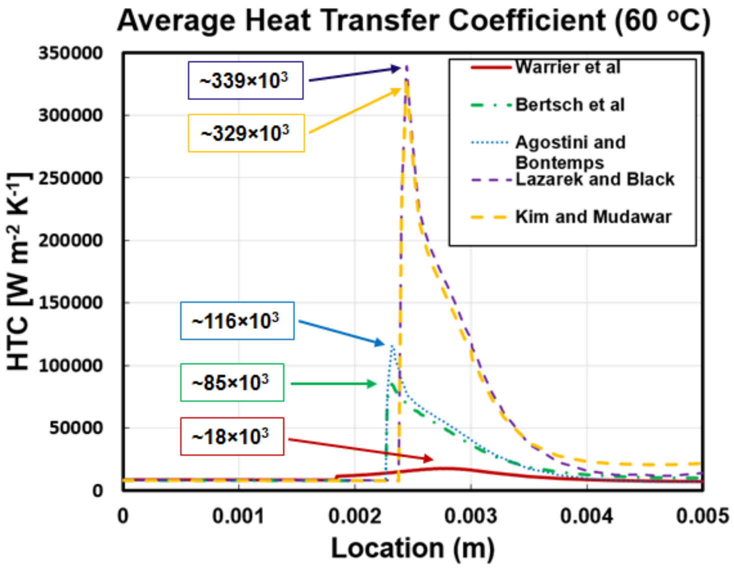

Figure 8. Average predicted heat transfer coefficients for the 60°C case.

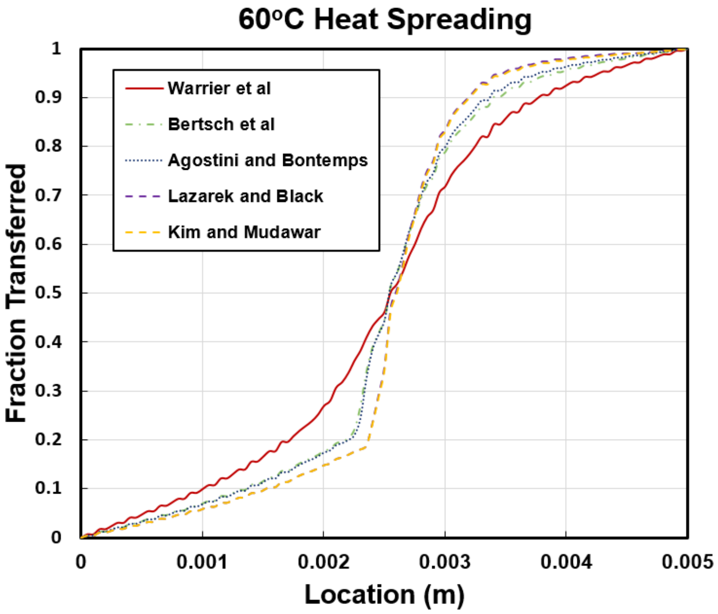

Figure 9. Predicted heat spreading for the 60°C case.

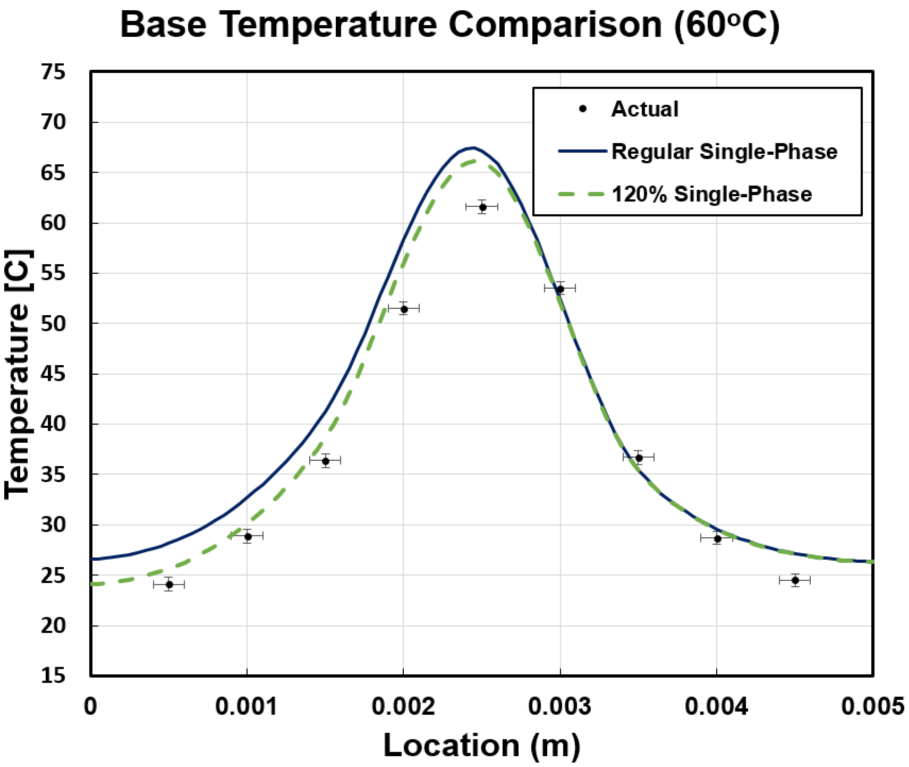

Figure 10. Experimental versus predicted base temperatures for the 60°C Agostini and Bontemps model with modified single-phase heat transfer coefficient.

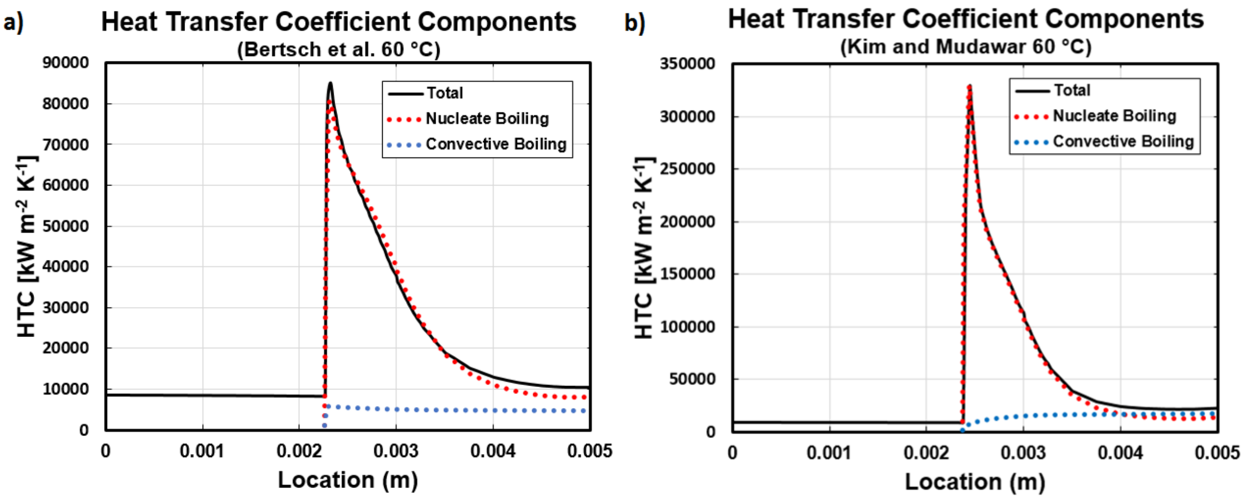

Figure 11. Comparison of nucleate and convective boiling contributions to total heat transfer coefficient for the (a) Bertsch et al. and (b) Kim and Mudawar 60°C nominal temperature models.

Tables

Table 1. Measured experimental parameters.

	Mass Flow Rate [g min^{-1}]	**Inlet Pressure [kPa]**	**Inlet Temperature [^{o}C]**	**Applied Heat Flux [kW m^{-2}]**
40°C	100.8	621.3	14.5	3643
50°C	99.8	623.1	14.5	6981
60°C	99.7	633.4	11.5	9934

Table 2. RMS difference values for predictions vs experimental measures.

Correlation	**40 ^{o}C**	**50 ^{o}C**	**60 ^{o}C**	**Average**
	Total RMS Difference [^{o}C]			
Agostini and Bontemps	2.1	2.1	4.0	2.7
Bertsch et al	2.7	2.6	4.5	3.3
Kim and Mudawar	3.9	6.0	6.9	5.6
Lazarek and Black	3.8	5.8	6.3	5.3
Warrier et al	6.2	14.5	20.5	13.7
	Single Phase RMS Difference [^{o}C]			
Agostini and Bontemps	2.5	2.2	5.0	3.3
Bertsch et al	2.9	2.7	5.7	3.8
Kim and Mudawar	1.3	0.8	1.0	1.0
Lazarek and Black	0.7	1.0	1.0	0.9
Warrier et al	6.4	13.4	19.0	12.9
	Two Phase RMS Difference [^{o}C]			
Agostini and Bontemps	1.7	2.0	2.9	2.2
Bertsch et al	2.6	2.5	3.	2.8
Kim and Mudawar	5.6	8.0	9.2	7.6
Lazarek and Black	5.6	7.7	8.4	7.3
Warrier et al	6.1	15.3	21.7	14.3

Table 3. Percentage of total heat transfer in both the single- and two-phase regions.

Correlation	Single-Phase	Two-phase
	40 ^{o}C Heater	
Agostini and Bontemps	36.1	63.9
Bertsch et al.	36.9	63.1
Kim and Mudawar	38.2	61.8
Lazarek and Black	34.9	65.1
Warrier et al.	37.6	62.4
Average	**36.7**	**63.3**
	50 ^{o}C Heater	
Agostini and Bontemps	20.5	79.5
Bertsch et al.	20.6	79.4
Kim and Mudawar	28.1	71.9
Lazarek and Black	25.3	74.7
Warrier et al.	20.8	79.2
Average	**23.1**	**76.9**
	60 ^{o}C Heater	
Agostini and Bontemps	24.4	75.6
Bertsch et al.	26.9	73.1
Kim and Mudawar	23.4	76.6
Lazarek and Black	23.5	76.5
Warrier et al.	22.8	77.2
Average	**24.2**	**75.8**

Table 4. RMS difference values for Agostini and Bontemps model with altered single-phase heat transfer coefficient (modified by a factor of 1.2).

Heater Temp [^{o}C]	**Single-phase RMS [^{o}C]**	**Two-phase RMS [^{o}C]**	**Overall RMS [^{o}C]**
40	1.4	1.5	1.4
50	0.8	1.9	1.5
60	2.7	2.5	2.6

REFERENCES

[1] Tuckerman, D. B., and Pease, R. F. W., 1981, “High-Performance Heat Sinking for VLSI,” IEEE Electron Device Lett., **2**(5), pp. 126–129.

[2] Hamann, H. F., Weger, A., Lacey, J. A., Hu, Z., Cohen, E., and Wakil, J., 2007, “Hotspot-Limited Microprocessors: Direct Temperature and Power Distribution Measurements,” IEEE J. Solid-State Circuits, **42**(1), pp. 56–65.

[3] Mahajan, R., Chiu, C. P., and Chrysler, G., 2006, “Cooling a Microprocessor Chip,” Proc. IEEE, **94**(8), pp. 1476–1485.

[4] Costa-Patry, E., Nebuloni, S., Olivier, J., and Thome, J. R., 2012, “On-Chip Two-Phase Cooling with Refrigerant 85 Mm-Wide Multi-Microchannel Evaporator under Hot-Spot Conditions,” IEEE Trans. Components, Packag. Manuf. Technol., **2**(2), pp. 311–320.

[5] Tiwari, N., Moharana, M. K., and Sarangi, S. K., 2016, “Conjugate Heat Transfer in Single-Phase Wavy Microchannel,” Proc. ASME 2016 5th Int’l Conf. Micro/Nanoscale Heat Mass Transf., pp. 1–8.

[6] Nunes, J. S., Cotta, R. M., Avelino, M. R., and Kakac, S., 2010, “Conjugated Heat Transfer in Microchannels,” *Microfluidics Based Microsystems: Fundamentals and Applications*, pp. 61–82.

[7] Hannemann, R., Joseph, M., and Pitasi, M., 2004, “Pumped Liquid Multiphase Cooling,” *IMECE 2004*, pp. 3–7.

[8] Agostini, B., Fabbri, M., Park, J. E., Wojtan, L., Thome, J. R., and Michel, B., 2007, “State of the Art of High Heat Flux Cooling Technologies,” Heat Transf. Eng., **28**(4), pp. 258–281.

[9] Marcinichen, J. B., and Thome, J. R., 2010, “New Novel Green Computer Two-Phase Cooling Cycle: A Model for Its Steady-State Simulation,” Proc. 23rd Int. Conf. Effic. Cost, Optim. Simulation, Environ. Impact Energy Syst. ECOS 2010, **3**(January).

[10] Pan, Z., Weibel, J. A., and Garimella, S. V, 2015, “A Cost-Effective Modeling Approach for Simulating Phase Change and Flow Boiling in Microchannels,” *Proc. of ASME 2015 Int’l Technical Conf. and Exhibition on Packaging and Integration of Electronic and Photonic Microsystems,* San Francisco, CA, pp. 1–9.

[11] Mudawar, I., 2001, “Assessment of High-Heat-Flux Thermal Management Schemes,” Components Packag. Technol. IEEE Trans., **24**(2), pp. 122–141.

[12] Tran, T. N., Wambsganss, M. W., and France, D. M., 1996, “Small Circular- and Rectangular-Channel Boiling with Two Refrigerants,” Int. J. Multiph. Flow, **22**(3), pp. 485–498.

[13] Willingham, T. C., and Mudawar, I., 1992, “Forced-Convection Boiling and Critical Heat Flux from a Linear Array of Discrete Heat Sources,” Int. J. Heat Mass Transf., **35**(11), pp. 2879–2890.

[14] Agostini, B., Thome, J. R., Fabbri, M., and Michel, B., 2008, “High Heat Flux Two-Phase Cooling in Silicon Multimicrochannels,” IEEE Trans. Components Packag. Technol., **31**(3), pp. 691–701.

[15] Kim, S. M., and Mudawar, I., 2014, “Review of Databases and Predictive Methods for Heat Transfer in Condensing and Boiling Mini/Micro-Channel Flows,” Int. J. Heat Mass Transf., **77**, pp. 627–652.

[16] Bertsch, S. S., Groll, E. A., and Garimella, S. V, 2009, “A Composite Heat Transfer Correlation for Saturated Flow Boiling in Small Channels,” Int. J. Heat Mass Transf., **52**(7–

8), pp. 2110–2118.

[17] Li, W., and Wu, Z., 2010, “A General Correlation for Evaporative Heat Transfer in Micro/Mini-Channels,” Int. J. Heat Mass Transf., **53**(9–10), pp. 1778–1787.

[18] Mudawar, I., 2011, “Two-Phase Microchannel Heat Sinks: Theory, Applications, and Limitations,” J. Electron. Packag., **133**(4), pp. 041002-1-041002-31.

[19] Bertsch, S. S., Groll, E. a., and Garimella, S. V, 2008, “Review and Comparative Analysis of Studies on Saturated Flow Boiling in Small Channels,” Nanoscale Microscale Thermophys. Eng., **12**(3), pp. 187–227.

[20] Garimella, S. V, and Sobhan, C. B., 2003, *Transport in Microchannels–a Critical Review*.

[21] Kandlikar, S. G., 2012, “History, Advances, and Challenges in Liquid Flow and Flow Boiling Heat Transfer in Microchannels: A Critical Review,” J. Heat Transfer, **134**(3).

[22] Thome, J. R., 2006, “State-of-the-Art Overview of Boiling and Two-Phase Flows in Microchannels,” Heat Transf. Eng., **27**(9), pp. 4–19.

[23] Kim, S. M., and Mudawar, I., 2014, “Review of Databases and Predictive Methods for Pressure Drop in Adiabatic, Condensing and Boiling Mini/Micro-Channel Flows,” Int. J. Heat Mass Transf., **77**, pp. 74–97.

[24] Kew, P. A., and Cornwell, K., 1997, “Correlations for the Prediction of Boiling Heat Transfer in Small Diameter Channels,” Appl. Therm. Eng., **17**, pp. 705–715.

[25] Kandlikar, S. G., and Grande, W. J., 2003, “Evolution of Microchannel Flow Passages - Thermohydraulic Performance and Fabrication Technology,” Heat Transf. Eng., **24**(1), pp. 3–17.

[26] Kuznetsov, V. V., Shamirzaev, A. S., Kozulin, I. a., and Kozlov, S. P., 2013, “Correlation of the Flow Pattern and Flow Boiling Heat Transfer in Microchannels,” Heat Transf. Eng., **34**(2–3), pp. 235–245.

[27] Mehendale, S. S., Jacobi, M. A., and Shah, R. K., 2000, “Fluid Flow and Heat Transfer at Micro- and Meso-Scales with Application to Heat Exchanger Design,” Appl. Mech. Rev., **53**(7), pp. 175–193.

[28] Mishima, K., and Hibiki, T., 1996, “Some Characteristics of Air-Water Two-Phase Flow in Small Diameter Vertical Tubes,” Int. J. Multiph. Flow, **22**(4), pp. 703–712.

[29] Vlasie, C., Macchi, H., Guilpart, J., and Agostini, B., 2004, “Flow Boiling in Small Diameter Channels ´ Bullition Dans Des Canaux de Petit Diame ` Tre Ecoulement En E,” **27**, pp. 191–201.

[30] Dupont, V., and Thome, J. R., 2005, “Evaporation in Microchannels: Influence of the Channel Diameter on Heat Transfer,” Microfluid. Nanofluidics, **1**(2), pp. 119–127.

[31] Lazarek, G. M., and Black, S. H., 1982, “Evaporative Heat Transfer, Pressure Drop and Critical Heat Flux in a Small Vertical Tube with R-113,” Int. J. Heat Mass Transf., **25**(7), pp. 945–960.

[32] Owhaib, W., Martín-Callizo, C., and Palm, B., 2004, “Evaporative Heat Transfer in Vertical Circular Microchannels,” Appl. Therm. Eng., **24**(8–9), pp. 1241–1253.

[33] Sumith, B., Kaminaga, F., and Matsumura, K., 2003, “Saturated Flow Boiling of Water in a Vertical Small Diameter Tube,” Exp. Therm. Fluid Sci., **27**(7), pp. 789–801.

[34] Triplett, K. A., Ghiaasiaan, S. M., Abdel-Khalik, S. I., and Sadowski, D. L., 1999, “Gas–liquid Two-Phase Flow in Microchannels Part I: Two-Phase Flow Patterns,” Int. J. Multiph. Flow, **25**(3), pp. 377–394.

[35] Warrier, G. R., Dhir, V. K., and Momoda, L. A., 2002, “Heat Transfer and Pressure Drop in Narrow Rectangular Channels,” Exp. Therm. Fluid Sci., **26**(1), pp. 53–64.

[36] Qu, W., and Mudawar, I., 2003, “Flow Boiling Heat Transfer in Two-Phase Micro-Channel Heat Sinks—I. Experimental Investigation and Assessment of Correlation Methods,” Int. J. Heat Mass Transf., **46**(15), pp. 2755–2771.

[37] Thome, J. R., 2004, “Boiling in Microchannels: A Review of Experiment and Theory,” Int. J. Heat Fluid Flow, **25**(2), pp. 128–139.

[38] Szczukiewicz, S., Magnini, M., and Thome, J. R., 2014, “Proposed Models, Ongoing Experiments, and Latest Numerical Simulations of Microchannel Two-Phase Flow Boiling,” Int. J. Multiph. Flow, **59**, pp. 84–101.

[39] Magnini, M., Pulvirenti, B., and Thome, J. R., 2013, “Numerical Investigation of Hydrodynamics and Heat Transfer of Elongated Bubbles during Flow Boiling in a Microchannel,” Int. J. Heat Mass Transf., **59**(1), pp. 451–471.

[40] Zhuan, R., and Wang, W., 2012, “Flow Pattern of Boiling in Micro-Channel by Numerical Simulation,” Int. J. Heat Mass Transf., **55**(5–6), pp. 1741–1753.

[41] Mukherjee, A., and Kandlikar, S. G., 2005, “Numerical Simulation of Growth of a Vapor Bubble during Flow Boiling of Water in a Microchannel,” Microfluid. Nanofluidics, **1**(2), pp. 137–145.

[42] Li, D., and Dhir, V. K., 2007, “Numerical Study of Single Bubble Dynamics During Flow Boiling,” J. Heat Transfer, **129**(7), p. 864.

[43] Knupp, D. C., Naviera Cotta, C. P., and Cotta, R. M., 2012, “Conjugated Heat Transfer in Micro-Channels with a Single Domain Formulation and Integral Transforms,” *Proc. of ASME 2012 3rd Micro/Nanoscale Heat and Mass Transfer Conference*, Atlanta, GA.

[44] Knupp, D. C., Cotta, R. M., and Naveira Cotta, C. P., 2013, “Conjugated Heat Transfer in Heat Spreaders with Micro-Channels,” *Proc. of ASME 2013 Heat Transfer Summer Conference*.

[45] Magnini, M., Pulvirenti, B., and Thome, J. R., 2013, “Numerical Investigation of the Influence of Leading and Sequential Bubbles on Slug Flow Boiling within a Microchannel,” Int. J. Therm. Sci., **71**, pp. 36–52.

[46] Zhang, P., and Jia, H. W., 2016, “Evolution of Flow Patterns and the Associated Heat and Mass Transfer Characteristics during Flow Boiling in Mini-/Micro-Channels,” Chem. Eng. J., **306**, pp. 978–991.

[47] Tibiriçá, C. B., and Ribatski, G., 2014, “Flow Patterns and Bubble Departure Fundamental Characteristics during Flow Boiling in Microscale Channels,” Exp. Therm. Fluid Sci., **59**, pp. 152–165.

[48] Pellicone, D., Ortega, A., del Valle, M., and Schon, S., 2011, “Simulation of Two-Phase Flow and Heat Transfer in Mini-and Micro-Channels for Concentrating Photovoltaics Cooling,” *ASME 2011 5th International Conference on Energy Sustainability*, pp. 1957–1965.

[49] Bandhauer, T. M., and Bevis, T. A., 2017, “High Heat Flux Boiling Heat Transfer For Laser Diode Arrays,” *Proc. of ASME 2016 14th Int’l Conf. on Nanochannels, Microchannels, and Minichannels*, ASME, Washington, DC.

[50] Bevis, T. A., 2016, “High Heat Flux Phase Change Thermal Management of Laser Diode Arrays,” Colorado State University.

[51] Kos¸ar, A., Kuo, C.-J. J., Peles, Y., Koşar, A., Kuo, C.-J. J., and Peles, Y., 2006, “Suppression of Boiling Flow Oscillations in Parallel Microchannels With Inlet Restrictors,” ASME J. Heat Transf., **128**(3), pp. 251–260.

[52] Kandlikar, S. G., Kuan, W. K., Willistein, D. a., and Borrelli, J., 2006, “Stabilization of

Flow Boiling in Microchannels Using Pressure Drop Elements and Fabricated Nucleation Sites," J. Heat Transfer, **128**(4), p. 389.

[53] Park, J. E., Thome, J. R., and Michel, B., 2009, "Effect of Inlet Orifice on Saturated CHF and Flow Visualization in Multi-Microchannel Heat Sinks," Annu. IEEE Semicond. Therm. Meas. Manag. Symp., pp. 1–8.

[54] Costa-Patry, E., Olivier, J., Michel, B., and Thome, J. R., 2011, "Two-Phase Flow of Refrigerants in 85 Mm-Wide Multi-Microchannels: Part II – Heat Transfer with 35 Local Heaters," Int. J. Heat Fluid Flow, **32**(2), pp. 464–476.

[55] "Comsol Multiphysics^{TM} v. 4.4."

[56] Agostini, B., and Bontemps, A., 2005, "Vertical Flow Boiling of Refrigerant R134a in Small Channels," Int. J. Heat Fluid Flow, **26**(2), pp. 296–306.

[57] Cooper, M. G., 1984, *Heat Flow Rates in Saturated Nucleate Pool Boiling – a Wide-Ranging Examination Using Reduced Properties*.

[58] Hausen, H., 1943, "Darstellung Des Wärmeüberganges in Rohren Durch Verallgemeinerte Potenzbeziehungen," Z. VDI Beih. Verfahrenstechnik, **4**, pp. 91–102.

[59] Schrock, V. ., and Grossman, L. ., 1962, "Forced Convection Boiling in Tubes," Nucl. Sci. Eng., **12**(4), pp. 474–482.

[60] Kim, S. M., and Mudawar, I., 2012, "Consolidated Method to Predicting Pressure Drop and Heat Transfer Coefficient for Both Subcooled and Saturated Flow Boiling in Micro-Channel Heat Sinks," Int. J. Heat Mass Transf., **55**(13–14), pp. 3720–3731.

[61] Shah, R. K., and London, A. L., 1978, *Laminar Flow Forced Convection in Ducts*, Academic Press.

[62] Copeland, D., 1995, "Manifold Microchannel Heat Sinks: Analysis and Optimization," *ASME/JSME Thermal Engeering*, pp. 169–174.

[63] Churchill, S. W., 1977, *Friction-Factor Equation Spans All Fluid Flow Regimes*.

[64] Crane Co, 1979, "Flow of Fluids through Valves, Fittings and Pipes."

[65] Bevis, T., Burk, B., Hoke, J., Kotovsky, J., Hamilton, J., and Bandhauer, T. M., "Flow Boiling of R134a in a High Surface Area Microchannel Array for High-Flux Laser Diode Cooling," Heat Transf. Res.

[66] Lee, P.-S., and Garimella, S. V, 2008, "Saturated Flow Boiling Heat Transfer and Pressure Drop in Silicon Microchannel Arrays," Int. J. Heat Mass Transf., **51**(3–4), pp. 789–806.